



Full length article

Study on the structure, growth pattern and corrosion behavior of CoCrFeNiAl high entropy alloy coatings - base on hollow cathode effect

Dongbo Wei ^{a,b,*}, Zeyu Gao ^{a,b,*}, Xuming Lv ^c, Jianhua Liu ^{a,b}, Pingze Zhang ^{a,b}^a College of Materials Science and Technology, Nanjing University of Aeronautics and Astronautics, Nanjing 211106, China^b Materials Preparation and Protection for Harsh Environment Key Laboratory of Ministry of Industry and Information Technology, Nanjing 211106, China^c Science and Technology on Particle Transport and Separation Key National Defense Laboratory, Research Institute of Physical and Chemical Engineering of Nuclear Industry, Tianjin 300180, China

ARTICLE INFO

ABSTRACT

Keywords:

Hollow cathode effect
CoCrFeNiAl high entropy coating
Structure
Growth mode
Electrochemical corrosion in 3.5 wt% NaCl solution

The surface of TC18 titanium alloy was coated with a CoCrFeNiAl HEA coating using double-glow plasma surface metallurgy. The structure, phase, and growth mode of the coating were investigated, along with its electrochemical corrosion behavior. The prepared HEA coating, under the influence of the hollow cathode effect and non-equilibrium diffusion, exhibits a composite structure consisting of a deposited layer and an interdiffused layer. It demonstrates robust metallurgical bonding with the substrate, and it exhibits a hardness of 12.66 GPa and an elastic modulus of 158.52 GPa, along with exceptional hardness and high elastic modulus. The primary phase of the coating consists of an FCC solid solution, with a minor presence of Ni₃Al and Al₈Cr₅ phases. TEM results demonstrate that hollow cathode enhanced sputtering effectively refines the grain structure on the substrate surface. The high entropy alloy coating, characterized by a significant abundance of nanocrystalline and amorphous structures, is obtained under the bombardment of high-energy particles. Gradually increasing from the interface to the deposited layer, there is an augmentation in the content of nanocrystals. The transition from the substrate to the sedimentary layer comprises three distinct regions: a surface fine crystal region, a nanocrystalline structure region, and a nanocrystalline and amorphous precipitated phase-rich region. In 3.5 wt % NaCl solution, the electrochemical corrosion rate of the coating is $1.36 \times 10^{-1} \mu\text{m}\cdot\text{year}^{-1}$, which is about ten times lower than that of the substrate. Moreover, pre-soaking forms a stable oxide film on the coating's surface, effectively preventing corrosion and demonstrating its remarkable corrosion resistance.

1. Introduction

Due to its unique microstructure, exceptional mechanical, tribological, and corrosion resistance properties [1,2], high-entropy alloys have emerged as promising candidates for meeting the demands of challenging working conditions in harsh environments and are progressively gaining widespread utilization [3]. The concept of high entropy alloy was proposed and successfully synthesized by Yeh et al. [4,5] in 2004, challenging the conventional approach to alloy design based on one or two elements. Compared to conventional alloys, high entropy alloys exhibit four distinct effects: the high entropy effect in thermodynamics, the slow diffusion effect in dynamics, the lattice distortion effect in structure, and the “cocktail” effect in performance [6,7]. In recent years, extensive research has been conducted by numerous scholars on high-entropy alloys. Apart from the conventional methods of sintering [8]

and casting [9] to obtain bulk high-entropy alloys, surface technology has emerged as a potent approach for the preparation of high-entropy alloys, with current widespread exploration focusing on high-entropy films and coatings.

Surface modification technology enables the attainment of exceptional surface performance while preserving the inherent material properties. Numerous scholars have commenced fabricating high-entropy alloy coatings and employing high-entropy alloys for surface modification [10–13]. Currently, the predominant techniques employed for fabricating high-entropy alloy coatings encompass magnetron sputtering [14,15] and laser cladding [16,17], while some researchers utilize spraying [18,19] and electrochemical deposition [20,21], among other methods. Revised sentence: However, the preparation methods of these high-entropy coatings exhibit certain limitations. The electrochemical deposition process is susceptible to redox reactions, which can impact

* Corresponding authors at: College of Materials Science and Technology, Nanjing University of Aeronautics and Astronautics, Nanjing 211106, China.

E-mail addresses: weidongbo@nuaa.edu.cn (D. Wei), gaozeyu@nuaa.edu.cn (Z. Gao).

the performance of the deposited layer. Additionally, cracks or precipitates may arise within the deposited layer, thereby potentially compromising its quality. Additionally, laser cladding equipment is costly and operates at excessively high temperatures during the working process.

The double glow plasma surface metallurgy technology (referred to as double glow technology) [22,23] is an innovative technique in plasma surface alloying that has been developed based on ion nitriding. This breakthrough overcomes the limitations previously restricted to a few non-metallic elements and enables the preparation of single and multiple alloy coatings on metal surfaces. The Double Glow Technology (as illustrated in Fig. 1) involves the placement of dual cathode plates within a vacuum chamber and the application of varying negative voltages to establish a potential difference, thereby inducing the hollow cathode effect. This effect enhances glow discharge and facilitates sputtering elements to permeate, resulting in alloying on the substrate surface and diffusion into the substrate. Consequently, a high-performance permeable coating with gradient distribution of elements is formed, exhibiting strong metallurgical bonding with the substrate. Resulting in alloying on the substrate surface and diffusion into the substrate. Consequently, a high-performance permeable coating with gradient distribution of elements is formed, exhibiting strong metallurgical bonding with the substrate.

Researchers have demonstrated that high-entropy coatings possess significant potential for providing exceptional corrosion protection. Among various high-entropy alloy (HEA) systems, the AlCoCrFeNi series, composed of common elements such as Co, Cr, Fe, Ni and Al, has garnered considerable attention due to its remarkable combination of high yield strength, excellent structural stability at elevated temperatures and superior wear resistance [24–27]. The study conducted by Fan et al. [28] demonstrated a 20 % increase in microhardness and enhanced corrosion resistance of Q235 mild steel when coated with AlCoCrFeNi HEA. An isoatomic AlCoCrFeNi HEA coating was fabricated through atmospheric plasma spraying (APS) by Ashok Meghwal et al. [29], demonstrating exceptional thermal stability and corrosion resistance. The electrochemically deposited AlCoCrFeNi film, as reported by David Miklos Kemeny et al. [30], exhibited higher porosity compared to the copper substrate; however, it demonstrated superior corrosion resistance in a 3.5 % NaCl solution. The AlCoCrFeNi high-entropy alloy coating was prepared by Zhenzeng Chong et al. [31] using high-speed laser cladding (HLC) technology. The coating exhibited an 84 mV increase in self-corrosion potential and a one order of magnitude reduction in self-corrosion current density.

In conclusion, this study focuses on the preparation of a CoCrFeNiAl HEA coating on a TC18 titanium alloy substrate using double-glow technology, with detailed investigations into the growth mode and structure of the coating. Additionally, the corrosion resistance and

behavior in a 3.5 wt% NaCl solution were examined through electrochemical performance tests.

2. Experimental details

2.1. Substrate pretreatment and coating preparation

Using the double glow technology (Fig. 2), the shell was utilized as the anode, while a CoCrFeNiAl alloy with equal atomic ratio, prepared through melting, served as the source electrode (the first cathode) in a vacuum chamber. Simultaneously, TC18 titanium alloy (nominal composition Ti-5Al-5Mo-5 V-1Cr-1Fe) was employed as the workpiece electrode (the second cathode). The distance between the two cathode plates was set to 16 mm, with a source voltage of 900 V and a work pole voltage of 500 V. Deposition occurred over a period of three hours. Following the deposition process, a gradual reduction in voltage is implemented to sustain a faint glow as a preventive measure against oxidation. Subsequently, the sample is cooled to room temperature within the vacuum chamber for stress relief purposes. The glow discharge is observed between the two cathode plates, as depicted in Fig. 2. The applied potential difference induces the hollow cathode effect, thereby enhancing the sputtering effect and accelerating the surface alloying of metal elements. Consequently, this process leads to the successful synthesis of a high-entropy alloy coating. Additionally, the sputtering effect of the hollow cathode can induce non-equilibrium diffusion, leading to the formation of an interdiffusion layer on the surface. This phenomenon has the potential to generate novel structures and unexplored phases within the high entropy coating.

2.2. Microstructural characterisation

The phase structure of the alloy layer was determined using X-Ray Diffractometer (XRD, BrukerD8-ADVANCE). Test parameters included a scanning range from 20° to 90° with a step size of 0.02°, utilizing Cu-K α radiation ($\lambda = 0.15418$ nm), and a scanning rate of 1.5°/min.

The microscopic morphology of the CoCrFeNiAl high-entropy alloy layer was observed using a Scanning Electron Microscope (SEM, Hitachi S-4800). Additionally, the composition of the alloy layer was qualitatively and quantitatively analyzed using Energy Disperse Spectroscopy (EDS). The sampling position was determined using scanning electron microscopy (SEM), and the longitudinal section was precisely cut using focused ion beam (FIB) technology. The microstructure and growth mode of the coating were subsequently investigated using transmission electron microscopy (TEM).

2.3. Nanoindentation

The nano-hardness and elastic modulus of the TC18 substrate and CoCrFeNiAl high-entropy alloy layer were determined using the DUH-W201 nano-indenter. The diamond triangle cone indenter was selected with a maximum load of 150 mN, a loading speed of 1.3239 mN/s, and a load retention time of 15 s.

2.4. Corrosion performance test

The electrochemical corrosion behavior of TC18 titanium alloy and CoCrFeNiAl HEA coating in 3.5 % NaCl solution was investigated using a ZAHNER ENNIUM electrochemical workstation. The open-circuit potential, AC impedance spectrum, and potentiostatic polarization curve were measured. The fitting analysis was conducted using Zahner Analysis software. The test sample was immersed in the corrosion solution for a duration of one day, enabling a comparison of the influence of passivation film on corrosion resistance before and after immersion, thus providing closer approximation to real-world application environments.

The test duration was 3600 s with a sampling interval of 1 s. The AC impedance spectrum was measured under open circuit conditions,

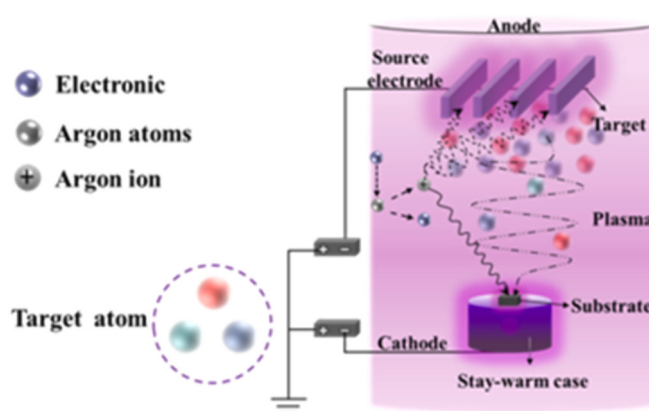


Fig. 1. Schematic diagram of coating preparation by dual-glow technique based on hollow cathode effect.



Fig. 2. Schematic diagram of dual glow technology equipment and glow discharge diagram of coating preparation process.

within the frequency range of 10^{-2} – 10^{-5} Hz, using an AC excitation signal amplitude of 5 mV. Potentiodynamic polarization curve testing involved voltage scanning from -0.5 V to $+0.5$ V (relative to the open circuit potential) at a scanning rate of 1 mV/s.

3. Results and discussion

3.1. Microstructural characterisation

The XRD diffraction pattern of the CoCrFeNiAl high entropy alloy layer prepared on the TC18 titanium alloy surface is presented in Fig. 3. It can be observed that the high entropy alloy coating primarily consists of a face-centered cubic (FCC) solid solution phase, with a lattice constant of 3.572 Å. The lattice constant of the face-centered cubic phase formed by most Fe, Co, Cr, Al and Ni elements exhibits similarity to that observed in the coating. Additionally, under the influence of non-equilibrium diffusion resulting from hollow cathode effect, the formation of Ni₃Al phase with space group Pm3m(221) and Al₈Cr₅ phase with space group R3m(160) is also observed in the coating. Notably, some diffraction peaks from these phases partially coincide with those of the main structural phases.

The Ni₃Al phase is classified as an ordered L₁₂ intermetallic compound with a face-centered cubic (FCC) structure. It has been observed that the L₁₂ phase exhibits exceptional strength, excellent wear resistance, and corrosion resistance, making it a preferred strengthening component in superalloys. The L₁₂ precipitation-enhanced high-entropy alloys (HEAs) have been developed by combining the advantages of

HEAs and L₁₂ ordered intermetallic compounds, demonstrating exceptional synergistic enhancement in strength and ductility [32]. Recently conducted studies have demonstrated that the incorporation of the L₁₂-phase structure can significantly enhance the strength of FCC HEAs, albeit at the expense of reduced plasticity [33]. Furthermore, it has been observed that L₁₂ precipitation-strengthened high-entropy alloys exhibit commendable thermal stability [34] and corrosion resistance [35]. The α -Al₈Cr₅ compound exhibits a rhomboid crystal structure, rendering it highly promising for research on Al–Cr intermetallic compounds due to its exceptional resistance to oxidation, corrosion, and thermal degradation. α -Al₈Cr₅ compound exhibits a rhomboid crystal structure, rendering it highly promising for research on Al–Cr intermetallic compounds due to its exceptional resistance to oxidation, corrosion, and thermal degradation [36,37]. In conclusion, these two intermetallic compounds play a pivotal role in enhancing the properties of the CoCrFeNiAl high entropy alloy layer.

The SEM morphology and element surface distribution of the CoCrFeNiAl high entropy alloy layer are depicted in Fig. 4. It is evident from the figure that the alloy layer exhibits a compact surface structure with a uniform distribution of each constituent element. Under the influence of hollow cathode sputtering and high-energy particle bombardment, the coating formed with microzone metal particles as its core aggregated and grew, exhibiting a characteristic “cellular bulge” morphology. Notably, the non-equilibrium sputtering induced by the hollow cathode effect resulted in an unequal atomic ratio within the coating. The literature studies [38,39] indicate that the effective solution concentration of aluminum is comparatively lower than that of other principal elements. A single-phase solid solution can only be formed within an Al content range between 6 at.% and 11 at.%. In this study, the coating's Al content was measured to be 16.74 at.%, exceeding the optimal range for single-phase solid solution formation. However, it should be noted that the presence of excess aluminum promotes the formation of precipitated phases containing aluminum, which does not pose a disadvantage.

The cross-sectional morphology and elemental line scanning distribution of the CoCrFeNiAl high entropy alloy layer are depicted in Fig. 5. The HEA coating exhibits a uniform and dense columnar crystal structure, growing outward from the substrate. This results in a robust metallurgical bond with the interface, as illustrated in Fig. 5(a). In conjunction with Fig. 5(b), region I corresponds to the deposition of a CoCrFeNiAl high-entropy alloy, exhibiting a thickness of approximately 5.3 μm. The grain structure of region II exhibits a higher level of refinement and densification compared to that of region I, displaying an approximately equiaxed morphology with a thickness measuring around 1.5 μm. Furthermore, the substrate (region III) demonstrates a close integration with the coating. The presence of a composition gradient transition between the high-entropy alloy (HEA) coating and the substrate effectively enhances the bonding strength between them.

The conditions for columnar grain growth are determined by the ratio of the substrate deposited element's melting point (T_m) to the substrate temperature (T_s), as well as the energy of plasma excitation

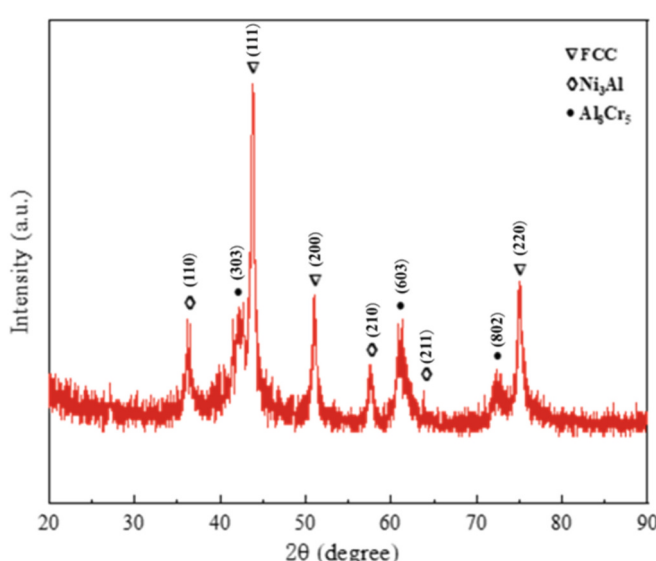


Fig. 3. XRD pattern of the CoCrFeNiAl HEA coating.

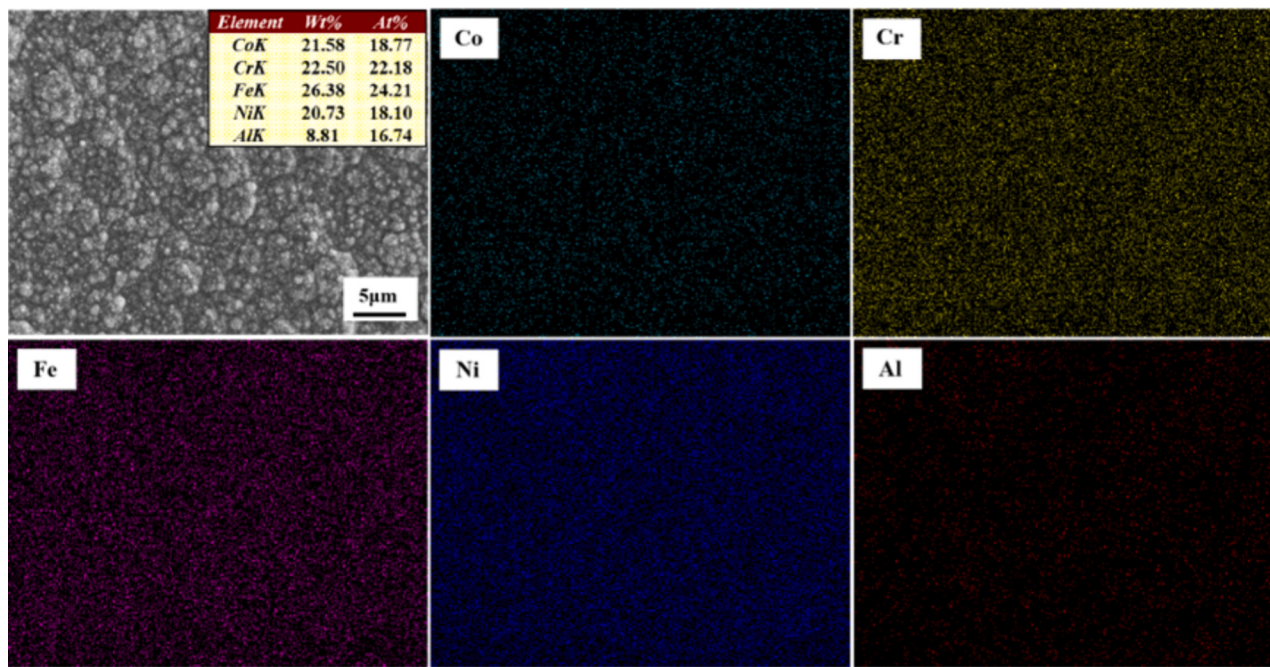


Fig. 4. Surface morphology and elemental surface distribution of CoCrFeNiAl high-entropy alloy layer.

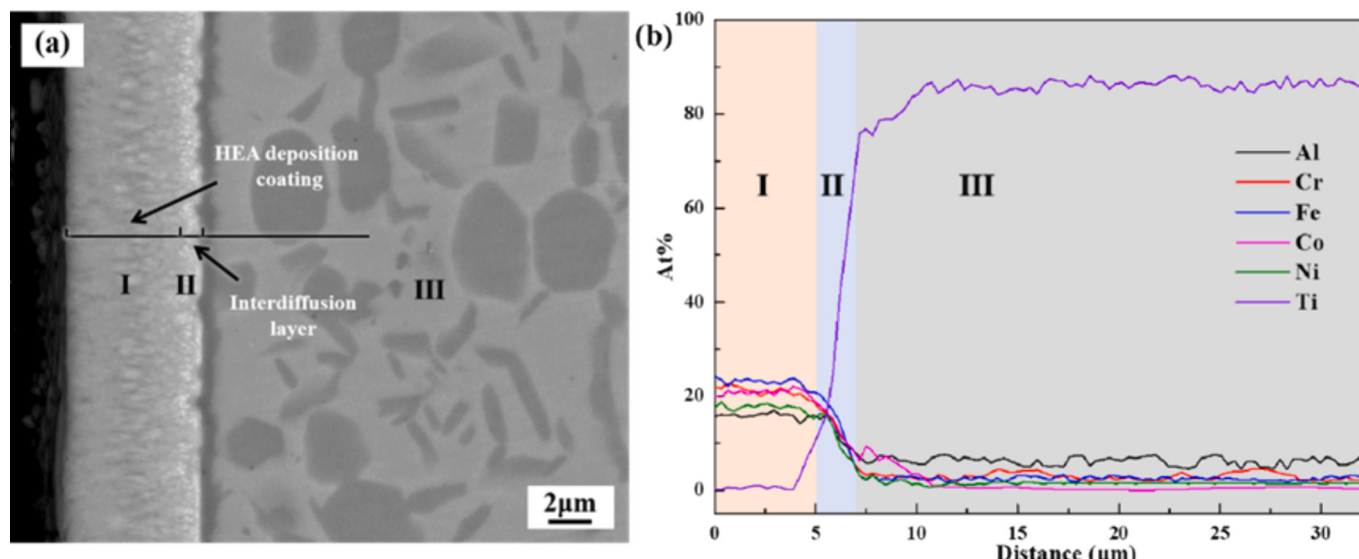


Fig. 5. Cross section morphology and elemental line scan of CoCrFeNiAl high entropy alloy layer.
(a) Cross section morphology; (b) EDS line scan element distribution.

(where pressure generally plays a significant role). When the relative temperature T_s/T_m is approximately 0.4, sufficient diffusion of infiltrated elements into the substrate occurs, resulting in a high-quality alloy layer formation. At this stage, crystal growth proceeds through columnar grain growth from inside to outside of the substrate. During CoCrFeNiAl high-entropy alloy coating preparation, due to higher control current applied on the substrate (cathode) compared to that on the target (source), there exists a temperature gradient with higher temperatures at and near the substrate surface than within other regions of coating deposition. This uniform temperature gradient and distribution of nucleation sites facilitate outwardly uniform growth from each nucleation site, leading to columnar grain formation.

Additionally, the CoCrFeNiAl high-entropy alloy layer can be categorized into three distinct regions: regional interface (I), interdiffusion

zone (II), and sedimentary layer (III). The corresponding TEM morphology and selected electron diffraction pattern are depicted in Fig. 6. The bonding state between the HEA coating and the substrate is well demonstrated in Fig. 6(a), with notable black nano-precipitates observed in the interdiffusion zone, which significantly contribute to enhancing the performance of the HEA coating. The electron diffraction patterns shown in Fig. b1 and b2 correspond to the diffusion region and the sedimentary layer. Both regions exhibit well-crystallized diffraction rings and partially bright diffraction spots, with slightly widened rings indicating a polycrystalline structure of the alloy layer comprising both nanocrystalline and amorphous structures. The diffraction patterns observed from the (111), (200), and (220) crystal surfaces suggest that the coating predominantly consists of face-centered cubic solid solution structural phases. The diffraction pattern of the sedimentary layer (Fig.

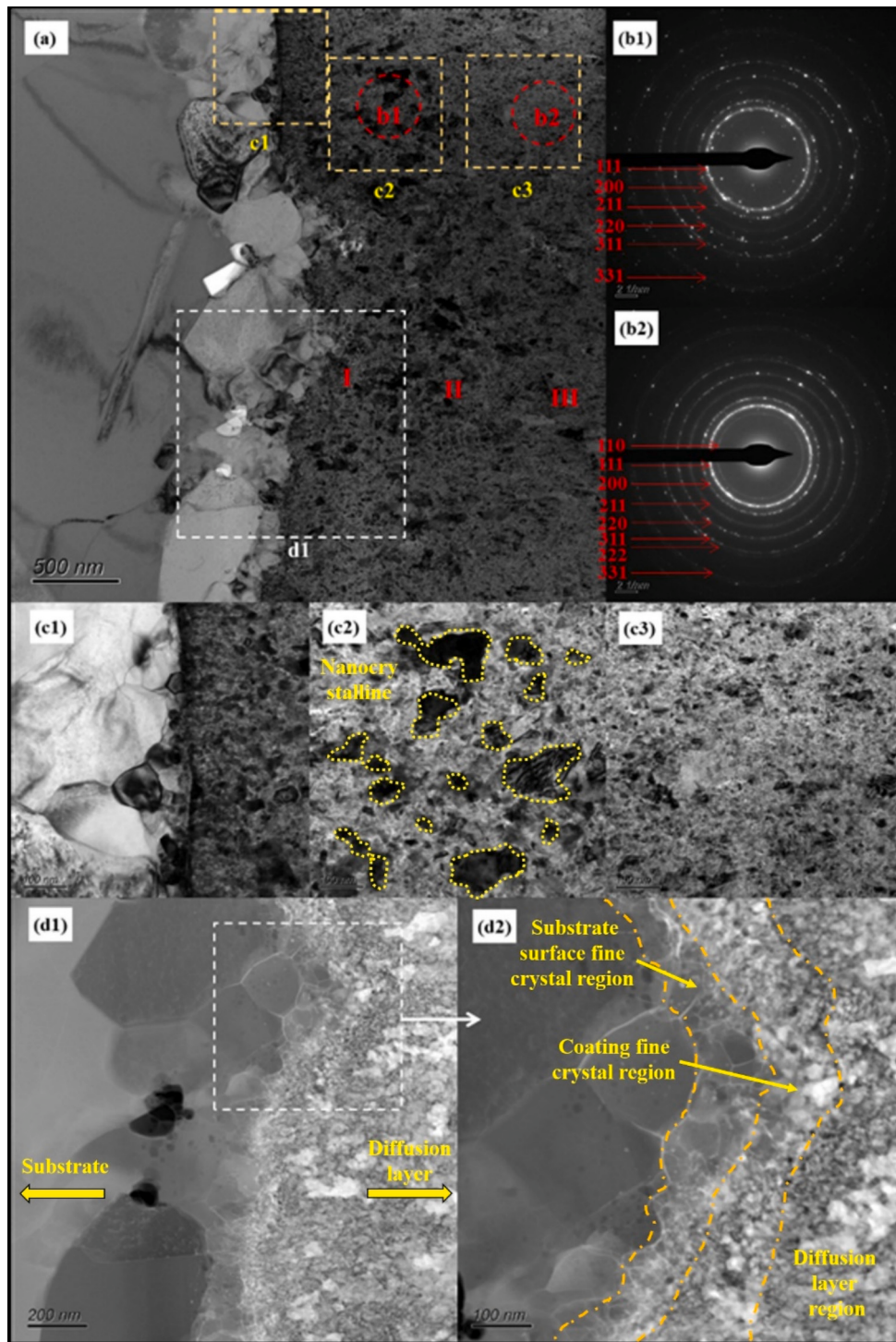


Fig. 6. Cross section morphology and corresponding selected area electron diffraction patterns of CoCrFeNiAl high entropy alloy layer.

b2) exhibits a higher level of continuity compared to that of the diffusion zone (Fig. b1), with more distinct and well-defined diffraction rings, indicating an enhanced degree of crystallization. The diffraction rings correspond to the crystal faces of (110), (211), and (311), while the non-coincident diffraction rings correspond to the crystal faces of (222) and (331). These observations suggest the presence of FCC nanocrystals with a highly refined FeNi structure in the coating.

The high-power TEM bright field images corresponding to the interface, the interdiffusion zone, and the deposited layer are shown in Fig. c1, c2, and c3 respectively. The coating exhibits a dense microstructure. Due to the distinct growth environments during different time

periods, diverse microstructures were formed in each region. The interfacial microstructure exhibits fine characteristics with the formation of black nano phases, while grain growth occurs within the interdiffusion zone. Additionally, the sedimentary layer contains dispersed nano precipitates with sizes ranging from approximately 10 to 50 nm.

The coating properties are closely associated with the interfacial morphology. HAADF-STEM images at different magnifications, as shown in Fig. d1 and d2. It is evident that a gradient transition of “substrate grain refinement region - diffusion region fine organization region - diffusion region precipitation rich region” is observed at the interface. The substrate surface was continuously bombarded with Ar^+

ions in this study to induce tissue defects and achieve a state of high temperature activation, while simultaneously promoting microstructure refinement to generate numerous nucleation centers. During the initial stage of the reaction, a relatively low temperature and slow supply of alloying elements resulted in smaller required nucleation work and critical nucleation radius for new grains on the surface of fine crystal layer, leading to the formation of equiaemic crystals. In the sedimentary layer region, the source electrode attains a stable and adequate supply state of elements, facilitating rapid adsorption and growth of alloy elements on the workpiece surface at a specific temperature. Consequently, an outward growth of columnar crystals occurs to form the desired structure. Due to the non-equilibrium sputtering of the hollow cathode effect, the nano-precipitated phase is dispersed within it. The simultaneous occurrence of metallurgical reactions induces a gradient change in grain size, which greatly enhances the bonding force of the coating. Moreover, its unique formation conditions provide an opportunity to

explore the generation of novel phases in high entropy alloys.

The HR-TEM high-resolution topography and Fourier transform diagram at the interface (region I) are presented in Fig. 7. Near the substrate interface, a significant grain refinement is observed, while near the alloy layer position, abundant nanocrystalline structures (dark regions) and amorphous structures (bright white regions) are formed, as depicted in Fig. 7a. The high-resolution topography analysis was conducted at three specific locations (1, 2, and 3) within the 200 nm range from the substrate to the alloy layer. The Fourier transform diagrams depicted in Fig. b1, b2, and b3 reveal that the transition from the substrate to the alloy layer is characterized by a shift from "nanocrystalline spots" to "nanocrystalline spots accompanied by amorphous halo rings." Additionally, Fig. c1, c2, and c3 exhibit detailed morphologies near the substrate (region 1), where both nanocrystalline structures and a minor proportion of amorphous structures are observed. At higher multiples, atoms exhibit short-range ordered structures, and the corresponding

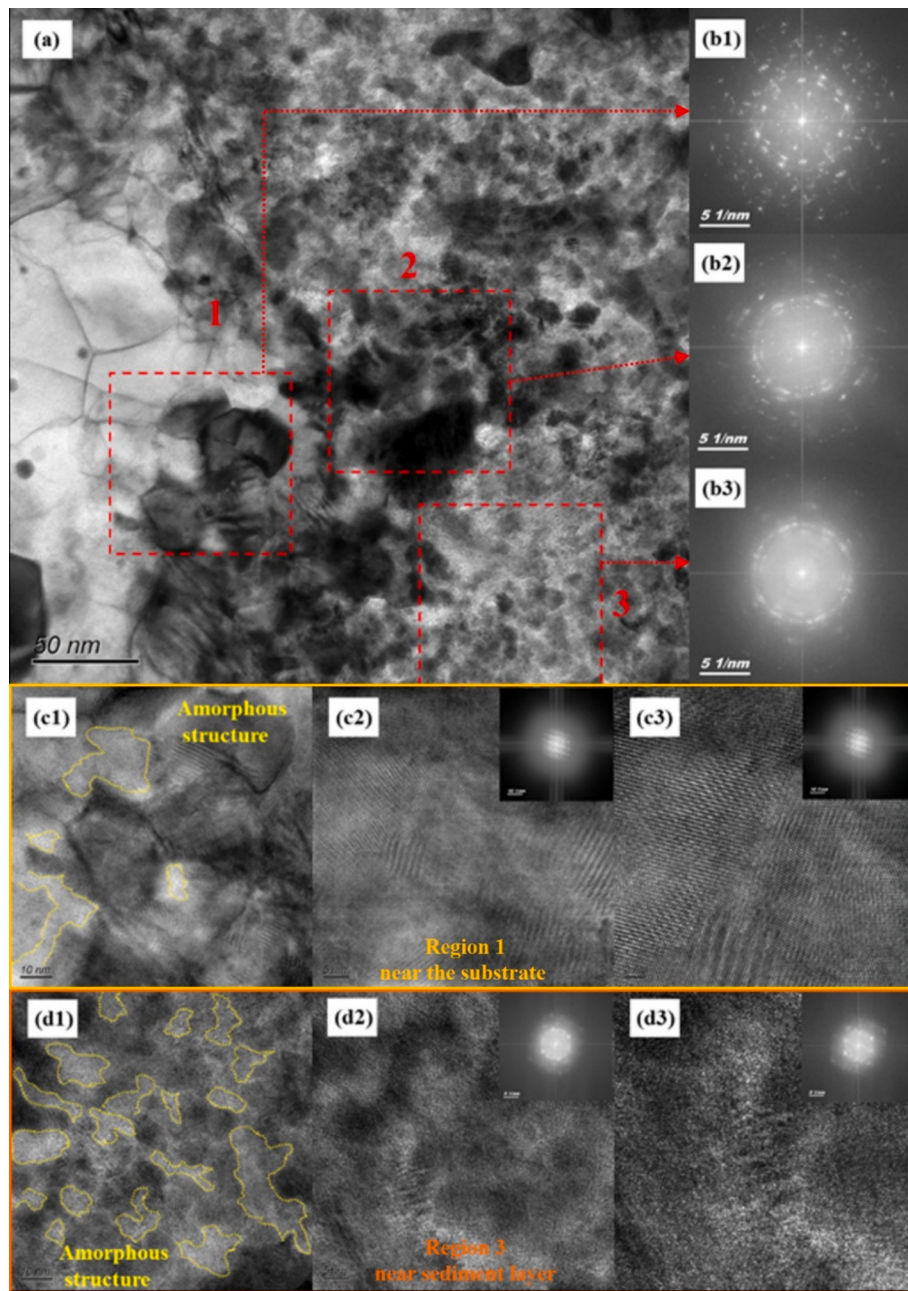


Fig. 7. HR-TEM high-resolution morphology and Fourier transform at the interface of CoCrFeNiAl high-entropy alloy layer.

Fourier transform reveals lattice diffraction spots associated with nanocrystalline formations. The high-resolution morphology near the sediment layer (region 3) is depicted in Fig. d1, d2, and d3. This region comprises nanocrystalline particles of size ranging from 5 to 10 nm along with amorphous structures. However, these constituents do not exhibit a uniform distribution of polarization, as evident from the corresponding Fourier transform that displays distinct characteristics of amorphous rings.

The sedimentary layer, as depicted in Fig. 8a, predominantly consists of uniformly dispersed nanocrystals and amorphous crystals. The Fourier transform diagrams of regions 1 and 2 (Fig. b1 and b2) provide evidence for the presence of continuous polycrystalline diffraction rings and amorphous halo rings in both locations. The high-resolution images of region 1, depicted in Fig. c1, c2, and c3, reveal predominantly short-range ordered structures among the atoms with a concurrent presence of highly chaotic local amorphous formations. The Fourier transform of the black precipitates reveals well-ordered nanocrystalline diffraction spots, indicative of nanocrystalline structures with a size of approximately 20 nm. High-resolution images (d1, d2, and d3) captured from region 2

exhibit slightly blurred diffraction rings, suggesting the presence of an amorphous component within the white region. The atomic arrangement in this area predominantly exhibits short-range order, forming a composite structure consisting of both nanocrystalline and amorphous phases. The Fourier transform diagram also reveals the enhanced visibility of nanocrystalline features within the micro-region.

3.2. Nano-indentation tests

The nanoindentation test is shown in Fig. 9. The HEA layer exhibits a smaller area enclosed by the curve and coordinate axis, demonstrating enhanced resistance to plastic deformation. The material's hardness is primarily influenced by its microstructure. Notably, the CoCrFeNiAl high-entropy coating based on the hollow cathode effect has witnessed significant improvement in hardness owing to pronounced lattice distortion resulting from mutual displacement of each constituent element. Simultaneously, the presence of numerous nanocrystalline structures within the CoCrFeNiAl high-entropy alloy layer has led to a remarkable strengthening effect through grain refinement. After the

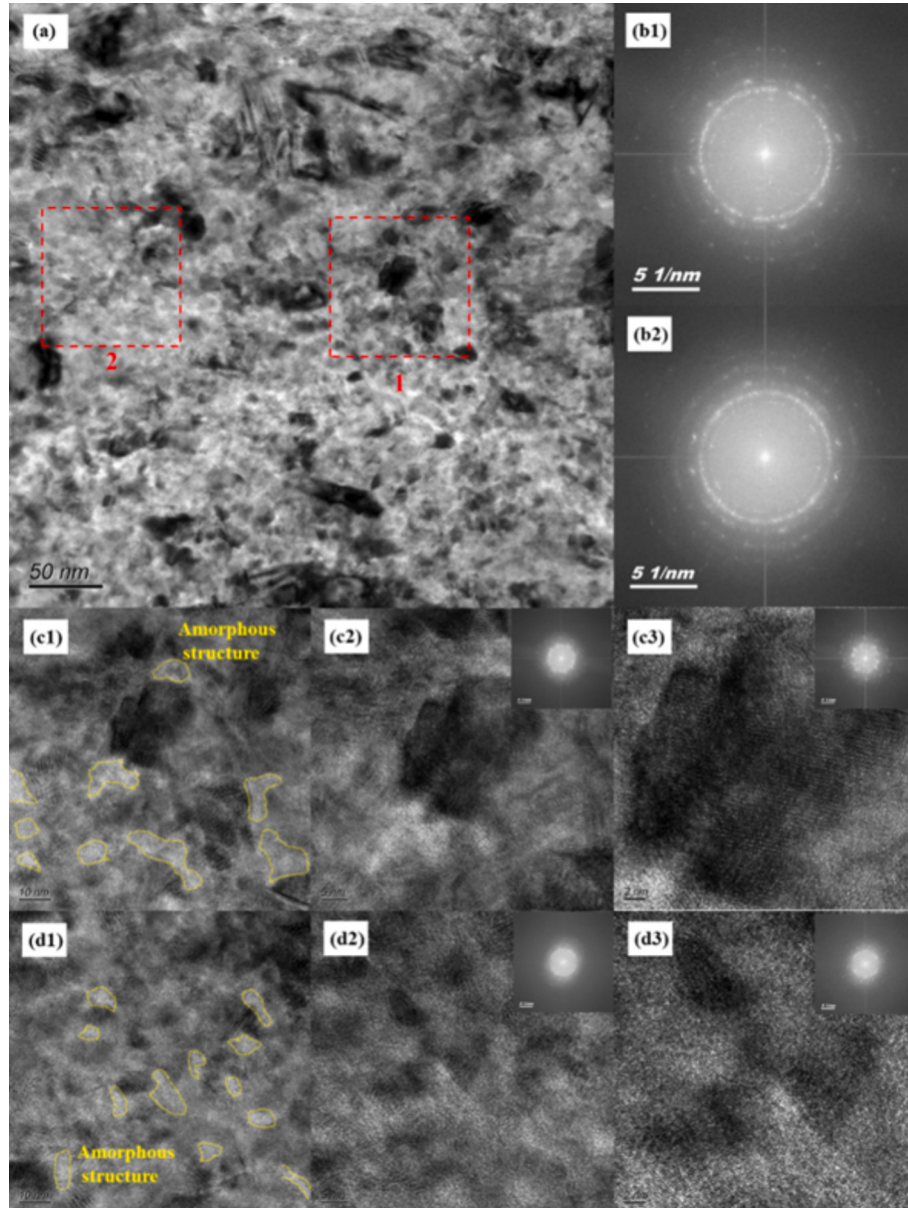
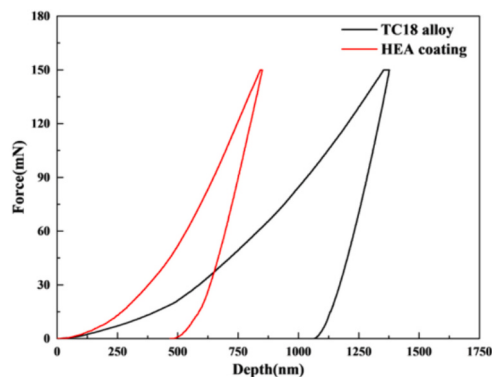


Fig. 8. HR-TEM high-resolution morphology and Fourier transform image of the deposition layer of CoCrFeNiAl high entropy alloy.



Samples	D (nm)	H (GPa)	E (GPa)	H/E	H^3/E^2
TC18	1376.24	4.02	96.12	0.042	0.007
HEA coating	849.99	12.66	158.52	0.080	0.081

Fig. 9. Load-displacement curves of TC18 titanium alloy substrate and CoCrFeNiAl high-entropy alloy layer and results.

preparation of a CoCrFeNiAl high-entropy alloy layer, the maximum surface pressing depth was found to be only 849.99 nm, with significantly improved nano hardness and elastic modulus compared to the substrate. The parameter H/E characterizes the resistance to elastic deformation of the sample, while H^3/E^2 represents its resistance to plastic deformation [40]. The calculation of test data reveals that the values of H/E and H^3/E^2 increase significantly from 0.042 to 0.080 and from 0.007 to 0.081, respectively, following the preparation of a CoCrFeNiAl high-entropy alloy layer. This observation underscores the exceptional resistance to both elastic deformation and plastic deformation exhibited by the CoCrFeNiAl high-entropy alloy layer.

3.3. Electrochemical corrosion of 3.5 wt% NaCl solution

The change curve of open circuit potential in a 3.5 % NaCl solution for TC18 titanium alloy and CoCrFeNiAl high-entropy alloy layer is presented in Fig. 10. It can be observed that TC18 consistently maintains a low open circuit potential, indicating its susceptibility to electrochemical corrosion. However, after 700 s of testing, the open circuit potential experiences a sharp decrease, suggesting that the passivation

layer only provides limited protection during the initial stages of corrosion. The HEA coating exhibited remarkable stability, and the formation of a surface oxide film during pre-soaking also contributed to the enhancement of open circuit potential. Moreover, the entire process remained stable within the range of 0.05 V to 0.10 V, indicating that the HEA coating possesses exceptional corrosion resistance and stability in saline environments.

The polarization curve of TC18 titanium alloy and CoCrFeNiAl high-entropy alloy layer in 3.5 % NaCl solution is presented in Fig. 11. After a one-day soaking period, the polarization potential of the alloy layer exhibited a slight decrease, while the polarization current significantly decreased, highlighting more pronounced passivation characteristics [41]. This observation further suggests that the soaking treatment can effectively mitigate the corrosion reaction tendency of HEA coating. In close proximity to the polarization potential, as the potential increases, an electric charge is induced at the interface between the sample and corrosion solution, leading to a sharp increase in current and initiation of passivation at the interface. As the voltage continues to increase, the passivated film undergoes a dynamic equilibrium between dissolution and self-healing. Conversely, when the current experiences spikes, it indicates an interruption in the passivated film on the sample's surface, leading to pitting and entry into an over-passivated zone [42,43]. The passivation behavior of TC18 and HEA coatings exhibited similarity during the potentiodynamic polarization test. However, the integrity of the passivation film and repair speed significantly influenced the corrosion process of the samples. The passivation zone curve reveals that the CoCrFeNiAl high-entropy alloy layer exhibits a reduced dimensional passivation current and an elevated rupture potential. After undergoing a 24-h soaking treatment, the CoCrFeNiAl high-entropy alloy layer exhibited the formation of a secondary passivation zone upon scanning to high potential [44,45]. This observation suggests that the passivation film in the passivation state demonstrates enhanced stability and repair capability. The alloy layer exhibits low surface activity and corrosion tendency due to its predominantly FCC solid solution structure, dense composition, and significant presence of nanocrystalline and amorphous structures.

The polarization curve fitting was performed using Zahner Analysis software, yielding the corrosion data for TC18 titanium alloy and CoCrFeNiAl high-entropy alloy layer, as presented in Table 1. The corrosion tendency of the HEA coating increases to a certain extent after immersion; however, it consistently remains significantly lower than that of TC18. The corrosion current density serves as an indicator for evaluating the severity of the material's corrosion reaction in solution. The electrochemical corrosion current of TC18 and HEA coatings

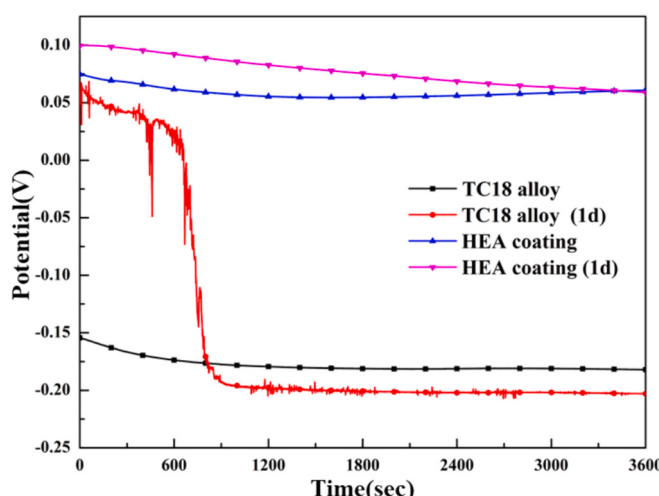


Fig. 10. Open circuit potential curves of TC18 titanium alloy and CoCrFeNiAl high entropy alloy layers in 3.5 % NaCl solution.

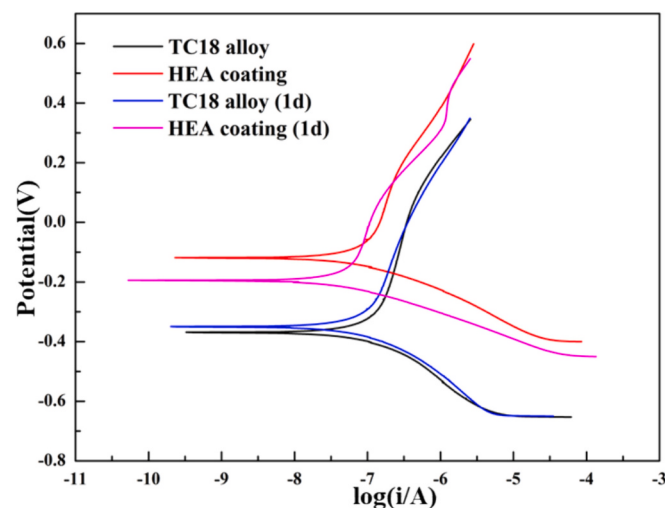


Fig. 11. Polarization curves of TC18 titanium alloy and CoCrFeNiAl high entropy alloy layers in 3.5 % NaCl solution.

Table 1

polarization curve fitting calculation results in 3.5 % NaCl solution.

	I_{corr} (nA·cm $^{-2}$)	E_{corr} (mV)	R_p (k Ω)	Corrosion rate ($\mu\text{m} \cdot \text{year}^{-1}$)
TC18 Substrate	184	-370	389	1.63
TC18 Substrate (1d)	136	-373	446	1.18
HEA coating	111	-119	388	1.36×10^{-1}
HEA coating (1d)	55.8	-196	577	4.76×10^{-1}

decreased after a 1-day soaking period, indicating that the formation of a passivation film reduced the severity of corrosion. The corrosion current density of the HEA layer was lower, suggesting its ability to maintain a more stable state and exhibit lower intensity in terms of corrosion reaction in NaCl salt solution. The polarization resistance R_p quantifies the resistance factor associated with the corrosion reaction occurring on the surface of the specimen. The polarization resistance values of TC18 and HEA layers exhibit close proximity prior to immersion; however, both experience a significant increase post-immersion, indicating the likelihood of surface passivation. Notably, the equivalent resistance value of the HEA coating surpasses that of TC18 after immersion. The results demonstrate that the passivation film formed by the HEA layer exhibits excellent quality and exerts a pronounced protective effect.

The calculated corrosion rate demonstrates a significantly low level for the CoCrFeNiAl high-entropy alloy layer, measuring 1.36×10^{-1} $\mu\text{m} \cdot \text{year}^{-1}$ and 4.76×10^{-1} $\mu\text{m} \cdot \text{year}^{-1}$ before and after immersion, respectively. This reduction in corrosion rate is an order of magnitude lower than that observed for the TC18 titanium alloy, effectively mitigating sample corrosion. This study presents a novel approach for the development of high entropy alloy coatings suitable for marine environments, offering a valuable contribution to the field.

The corrosion behavior of the HEA coating and TC18 titanium alloy substrate in 3.5 wt% NaCl solution was investigated by Nyquist and Bode diagrams, as illustrated in Fig. 12. The surface capacitive reactance responses of all test samples exhibit a single capacitive reactance arc, as depicted in Fig. 12a, with the center of the circle positioned below the X-axis. This characteristic is commonly associated with charge transfer on a non-uniform surface, indicating similarity among the surface capacitive reactance behaviors [38]. The high frequency component of the spectrum is typically associated with the barrier properties of the alloy layer, whereas the low frequency component reflects the corrosion reaction activity of the metal surface [47]. In the absence of soaking treatment, the arc radius of bulk reactance in TC18 and HEA layers exhibits similarity; however, at high frequencies, the arc amplitude of bulk reactance in the HEA layer surpasses that of the substrate significantly, indicating a higher reaction resistance for the HEA layer in NaCl solution. For corrosion protection systems with active anti-corrosion components, the low-frequency impedance increases during immersion, and this increase may be attributed to the inhibitory substances released by the alloy layer that provide corrosion protection. The

breakdown of the oxide film formed by immersion leads to a decrease in impedance and an increase in corrosion activity [46]. After a 1-day soaking treatment, the arc radius of the bulk reactance in the TC18 titanium alloy substrate remained unchanged; however, the arc amplitude of the bulk reactance decreased. In contrast, both the arc radius and amplitude of the CoCrFeNiAl high-entropy alloy layer significantly increased. These findings suggest that after a 1-day soaking treatment, a stable oxide film could not form on the substrate to effectively delay corrosion processes. The oxide film formed on the surface of the alloy layer after a 1-day immersion exhibits remarkable stability, effectively mitigating the corrosion reactivity of the sample. This finding aligns consistently with our previous analysis.

According to the Bode diagram (Fig. 12b), in the absence of soaking treatment, the phase angle of the substrate exhibits a slightly higher value compared to that of the HEA layer in the low frequency region. With the increase in scanning frequency, the phase angle of the alloy layer exhibits a slower decrease, indicating a delayed onset of corrosion activity in the HEA layer. After a 24-h immersion, the phase angle of the substrate and HEA layer exhibited an increase. Generally, the diameter of the semicircle is indicative of both charge transfer reactions occurring at the sample surface and the mass of the passivation film. In other words, a larger semicircle diameter corresponds to enhanced corrosion resistance [48]. Similarly, the maximum phase angle reflects the capacitive behavior of the impedance, indicating that a higher phase angle value corresponds to enhanced insulation performance. Therefore, the sample was pre-soaked for 24 h to facilitate the formation of a protective passivation film. The surface condition of the sample can be assessed based on the impedance amplitude observed in the Bode diagram. The amplitude of the CoCrFeNiAl high-entropy alloy layer is greater, indicating that the HEA layer can form a denser and more stable surface oxide film. After 1-day of soaking, the impedance amplitude of the substrate decreased while that of the alloy layer increased, suggesting a decrease in the density of the oxide film structure on the substrate surface after soaking for one day. However, the HEA layer maintained a dynamic equilibrium with its corrosion environment during soaking. The impedance test revealed a more stable and dense oxide film on its surface, exhibiting minimal corrosion tendency.

The selection of the equivalent circuit was based on the characteristics observed in the AC impedance spectrum of the sample, and fitting of the measured AC impedance spectrum was performed using Zahner Analysis software. The AC impedance maps of TC18 titanium alloy and CoCrFeNiAl high-entropy alloy layer exhibit similar characteristics, thereby enabling the utilization of the same equivalent circuit fitting analysis. The selected equivalent circuit diagram is depicted in Fig. 13. During electrochemical testing, the presence of an oxide film often leads to a dispersion effect, causing the surface impedance of the sample to deviate from that of an ideal capacitance impedance. To account for this deviation, a constant phase element (CPE) is employed instead of a pure ideal capacitance [38]. The local impedance of CPE, denoted as Z_{CPE},

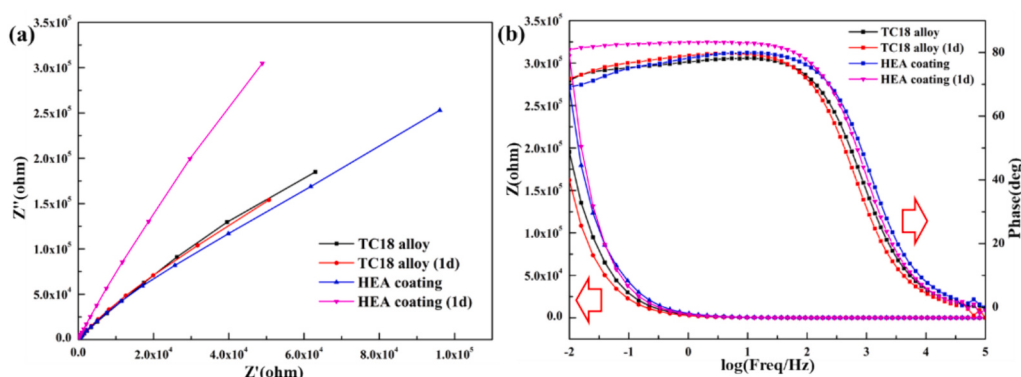


Fig. 12. AC impedance spectra of TC18 titanium alloy substrate and cocrfenal high entropy alloy layer in 3.5 % NaCl solution (a) Nyquist spectrum; (b) Bode Atlas.

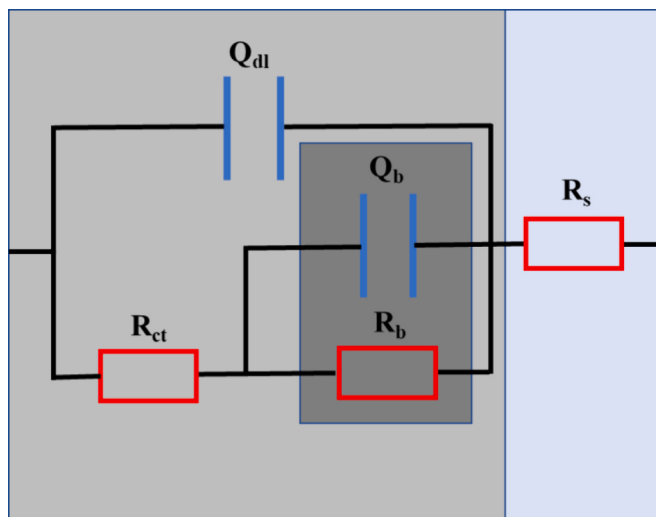


Fig. 13. AC impedance fitting equivalent circuit diagram of TC18 titanium alloy substrate and cocrfenal high entropy alloy layer.

can be mathematically expressed as follows.

$$Z_{CPE} = \frac{J\omega^{-n}}{Y_0} \quad (1)$$

The results of equivalent circuit fitting are presented in Table 2, with the fitting error being controlled within 5 %. It is observed that the oxidation film resistance (R_B) of TC18 and hea layers surpasses the charge transfer resistance (R_{CT}) by two to three orders of magnitude. This implies that the corrosion process of the sample is predominantly influenced by the state of the oxidation film formed on its surface. After immersion treatment, the resistance of the surface oxidation film R_B in TC18 decreased while the thickness of the hea layer increased. These observations suggest that the structure of the passive film on the surface of the hea layer remained stable after immersion treatment, thereby maintaining a high level of corrosion resistance. Additionally, irrespective of the implementation of pre-immersion treatment, the high entropy alloy layer exhibited superior resistance compared to TC18, thereby signifying a significant enhancement in the corrosion resistance of the substrate surface. Compared to the n value of Q_B , it can be observed that the substrate's n value slightly decreases after immersion, indicating the greater susceptibility of TC18 to deepening electrochemical corrosion due to passive film defects. Notably, the surface of hea layer without soaking treatment exhibits more "cellular growth" metal particles, resulting in a lower n value. However, after soaking treatment, there is a significant increase in the n value, suggesting the formation of a uniform and dense oxide film on the surface of cocrfenal high entropy alloy layer which effectively enhances its corrosion resistance.

4. Conclusions

The CoCrFeNiAl high entropy alloy coating on TC18 titanium alloy was successfully fabricated using the double-glow plasma surface metallurgy technique. Its structure, phase composition, growth mode, and

mechanical properties were comprehensively investigated. Finally, an in-depth analysis of its corrosion resistance was conducted, leading to the following conclusions:

- (1) Based on the hollow cathode effect, the CoCrFeNiAl high-entropy alloy layer exhibits a uniform and dense surface, primarily consisting of an FCC solid solution phase. Non-equilibrium sputtering conditions promote the formation of Ni₃Al and Al₈Cr₅ phases, thereby enhancing the performance of the alloy layer. The high entropy alloy layer has a thickness of approximately 6.8 μm, comprising a 5.3 μm sedimentary layer and a 1.5 μm interdiffusion layer characterized by gradient distribution of elements, ensuring strong metallurgical bonding between the coating and substrate.
- (2) The TEM results revealed the growth of columnar crystals in the coating, and the sputtering enhancement from the hollow cathode significantly refined the surface grains of the substrate. Upon high-energy particle bombardment, a high-entropy alloy coating with abundant nanocrystalline and amorphous structures was obtained. The nanocrystalline content gradually increases from the interface to the deposited layer, exhibiting a transition characterized by "surface fine crystal region - nanocrystalline structure region - nanocrystalline and amorphous precipitated phase-rich region". The deposited layer is predominantly composed of nanocrystalline structures ranging in size from 10 to 20 nm, accompanied by a minor fraction of amorphous structures.
- (3) The nanoindentation test reveals that the CoCrFeNiAl high-entropy alloy layer exhibits a hardness of 12.66 GPa and an elastic modulus of 158.52 GPa, demonstrating exceptional resistance to both elastic and plastic deformation. Moreover, it demonstrates remarkable load-bearing capacity and a high threshold for crack formation, thereby ensuring sufficient stability for practical applications of the coating.
- (4) Electrochemical tests in a 3.5 % NaCl solution revealed that the CoCrFeNiAl high-entropy alloy layer exhibited a higher corrosion potential and lower corrosion current. The corrosion rate of the alloy layer decreased to 0.08 and 0.4 times that of TC18 before and after soaking for one day, respectively. Ac impedance spectrum analysis demonstrated similar corrosion behavior between the substrate and the alloy layer, with the surface oxide film primarily contributing to corrosion resistance. However, the oxide film resistance on the surface of the alloy layer was found to be three to four times greater than that of the substrate. Following one day of soaking treatment, a stable oxide film formed on the coating's surface effectively enhanced its corrosion resistance.

CRediT authorship contribution statement

Dongbo Wei: Writing – review & editing, Supervision, Resources, Methodology, Investigation, Funding acquisition, Conceptualization. **Zeyu Gao:** Writing – review & editing, Writing – original draft, Visualization, Investigation, Formal analysis, Data curation. **Xuming Lv:** Writing – review & editing, Resources, Methodology, Funding acquisition, Conceptualization. **Jianhua Liu:** Writing – review & editing, Investigation, Data curation. **Pingze Zhang:** Supervision, Resources,

Table 2
AC impedance fitting results in 3.5 % NaCl solution.

	R_s ($\Omega \cdot \text{cm}^{-2}$)	R_{ct} ($\Omega \cdot \text{cm}^{-2}$)	Q_{dl} ($\mu\text{F} \cdot \text{cm}^{-2}$)	$Q_{dl} \cdot n$	R_b ($\Omega \cdot \text{cm}^{-2}$)	Q_b ($\mu\text{F} \cdot \text{cm}^{-2}$)	$Q_b \cdot n$
TC18 Substrate	8.79	7.73×10^3	50.0	0.90	3.63×10^6	13.2	0.66
TC18 Substrate (1d)	7.33	8.20×10^3	70.3	0.91	2.97×10^6	12.9	0.61
HEA coating	8.20	5.72×10^3	33.9	0.92	8.82×10^6	9.57	0.58
HEA coating (1d)	6.57	3.98×10^4	43.4	0.94	9.05×10^6	3.01	0.73

Conceptualization.

Declaration of competing interest

The authors declare that they have no known competing financial interests or personal relationships that could have appeared to influence the work reported in this paper.

Data availability

Data will be made available on request.

Acknowledgements

Fund: This project supported by open Project Research Funds for Science and Technology on Particle Transport and Separation Key National Defense Laboratory (2022-JCJQ-LB-004).

References

- [1] E.P. George, D. Raabe, R.O. Ritchie, High-entropy alloys, *Nat. Rev. Mater.* 4 (2019) 515–534, <https://doi.org/10.1038/s41578-019-0121-4>.
- [2] X. Zhang, V. Pelenovich, X. Zeng, Q. Wan, J. Liu, A. Pogrebnyak, Y. Guo, Y. Liu, Y. Lei, B. Yang, Unravel hardening mechanism of AlCrNbSiTi high-entropy alloy coatings, *J. Alloys Compd.* 965 (2023) 171222, <https://doi.org/10.1016/j.jallcom.2023.171222>.
- [3] Z. Tang, M.C. Gao, H. Diao, T. Yang, J. Liu, T. Zuo, Y. Zhang, Z. Lu, Y. Cheng, Y. Zhang, K.A. Dahmen, P.K. Liaw, T. Egami, Aluminum alloying effects on lattice types, microstructures, and mechanical behavior of high-entropy alloys systems, *Jom* 65 (2013) 1848–1858, <https://doi.org/10.1007/s11837-013-0776-z>.
- [4] J.W. Yeh, S.K. Chen, S.J. Lin, J.Y. Gan, T.S. Chin, T.T. Shun, C.H. Tsau, S.Y. Chang, Nanostructured high-entropy alloys with multiple principal elements: novel alloy design concepts and outcomes, *Adv. Eng. Mater.* 6 (2004) 299–303, <https://doi.org/10.1002/adem.200300567>.
- [5] B. Cantor, I.T.H. Chang, P. Knight, A.J.B. Vincent, Microstructural development in equiatomic multicomponent alloys, *Mater. Sci. Eng. A* 375–377 (2004) 213–218, <https://doi.org/10.1016/j.msea.2003.10.257>.
- [6] A.A. Ruktuev, D.V. Lazurenko, T.S. Ogneva, R.I. Kuzmin, M.G. Golkovski, I. A. Bataev, Structure and oxidation behavior of CoCrFeNiX (where X is Al, Cu, or Mn) coatings obtained by electron beam cladding in air atmosphere, *Surf. Coat. Technol.* 448 (2022) 128921, <https://doi.org/10.1016/j.surfcoat.2022.128921>.
- [7] W. Liu, C.T. Wang, S.C. Zhao, L. Chen, Y.T. Li, X. Jiang, Y.X. Leng, Enhancing wear resistance: in-situ ceramic phase precipitation for strengthening and toughening FeCoNiCrNx high-entropy alloy films, *Surf. Coat. Technol.* 478 (2024) 130466, <https://doi.org/10.1016/j.surfcoat.2024.130466>.
- [8] P.F. Zhou, D.H. Xiao, T.C. Yuan, Microstructure, mechanical and corrosion properties of AlCoCrFeNi high-entropy alloy prepared by spark plasma sintering, *Acta Metallurgica Sinica (English Letters)* 33 (2019) 937–946, <https://doi.org/10.1007/s40195-019-00962-8>.
- [9] K.V.S. Thurston, B. Gludovatz, A. Hohenwarter, G. Laplanche, E.P. George, R. O. Ritchie, Effect of temperature on the fatigue-crack growth behavior of the high-entropy alloy CrMnFeCoNi, *Intermetallics* 88 (2017) 65–72, <https://doi.org/10.1016/j.intermet.2017.05.009>.
- [10] Z. Qiu, P. Zhang, D. Wei, B. Duan, P. Zhou, Tribological behavior of CrCoNiAlTiY coating synthesized by double-glow plasma surface alloying technique, *Tribology International* 92 (2015) 512–518, <https://doi.org/10.1016/j.triboint.2015.07.038>.
- [11] W. Liao, S. Lan, L. Gao, H. Zhang, S. Xu, J. Song, X. Wang, Y. Lu, Nanocrystalline high-entropy alloy (CoCrFeNiAl0.3) thin-film coating by magnetron sputtering, *Thin Solid Films* 638 (2017) 383–388, <https://doi.org/10.1016/j.tsf.2017.08.006>.
- [12] F. Yang, L. Dong, X. Hu, X. Zhou, F. Fang, Z. Xie, J. Jiang, Microstructural features and tensile behaviors of a novel FeMnCoCr high-entropy alloys, *Mater. Lett.* 275 (2020) 128154, <https://doi.org/10.1016/j.matlet.2020.128154>.
- [13] P. Shi, Y. Yu, N. Xiong, M. Liu, Z. Qiao, G. Yi, Q. Yao, G. Zhao, E. Xie, Q. Wang, Microstructure and tribological behavior of a novel atmospheric plasma sprayed AlCoCrFeNi high entropy alloy substrate self-lubricating composite coatings, *Tribol. Int.* 151 (2020) 106470, <https://doi.org/10.1016/j.triboint.2020.106470>.
- [14] A. Jansson, L.Z. Medina, L. Lautrup, U. Jansson, Magnetron sputtering of the high entropy alloy CoCrFeMnNi on 316L: influence of substrate grain orientations, *Surf. Coat. Technol.* 466 (2023) 129612, <https://doi.org/10.1016/j.surfcoat.2023.129612>.
- [15] Y. Li, C. Wang, D. Ma, X. Zeng, M. Liu, X. Jiang, Y.X. Leng, Nano dual-phase CuNiTiNbCr high entropy alloy films produced by high-power pulsed magnetron sputtering, *Surf. Coat. Technol.* 420 (2021) 127325, <https://doi.org/10.1016/j.surfcoat.2021.127325>.
- [16] L. Zhicheng, K. Dejun, Effects of TiC mass fraction on microstructure, corrosive-wear and electrochemical properties of laser cladded CoCrFeNiMo high-entropy alloy coatings, *Tribology International* 186 (2023) 108640, <https://doi.org/10.1016/j.triboint.2023.108640>.
- [17] F. Alazzawi, H. Aghajani, A. Kianvash, Surface improvement of Ti-6Al-4V alloy by deposition of AlCrCoFeMnNi high entropy alloy using TiG process, *JOM* 76 (2024) 656–666, <https://doi.org/10.1007/s11837-023-06314-3>.
- [18] J. Zhu, X. Cheng, L. Zhang, X. Hui, Y. Wu, H. Zheng, Z. Ren, Y. Zhao, W. Wang, S. Zhu, X. Wang, Microstructures, wear resistance and corrosion resistance of CoCrFeNi high entropy alloys coating on AZ91 Mg alloy prepared by cold spray, *J. Alloys Compd.* 925 (2022) 166698, <https://doi.org/10.1016/j.jallcom.2022.166698>.
- [19] A. Meghwal, S. Singh, A. Anupam, H.J. King, C. Schulz, C. Hall, P. Munroe, C. Berndt, A.S.M. Ang, Nano- and micro-mechanical properties and corrosion performance of a HVOF sprayed AlCoCrFeNi high-entropy alloy coating, *J. Alloys Compd.* 912 (2022) 165000, <https://doi.org/10.1016/j.jallcom.2022.165000>.
- [20] A. Aliyu, C. Srivastava, Microstructure and corrosion properties of MnCrFeCoNi high entropy alloy-graphene oxide composite coatings, *Materialia* 5 (2019) 100249, <https://doi.org/10.1016/j.mtla.2019.100249>.
- [21] A. Aliyu, C. Srivastava, Microstructure-corrosion property correlation in electrodeposited AlCrFeCoNiCu high entropy alloys-graphene oxide composite coatings, *Thin Solid Films* 686 (2019) 137434, <https://doi.org/10.1016/j.tsf.2019.137434>.
- [22] Z. Xu, F.F. Xiong, Double glow plasma surface alloying/metallurgy technology, in: Z. Xu, F.F. Xiong (Eds.), *Plasma Surface Metallurgy: With Double Glow Discharge Technology—Xu-Tec Process*, Springer Singapore, Singapore, 2017, pp. 33–62, https://doi.org/10.1007/978-981-10-5724-3_4.
- [23] S. Yuan, N. Lin, Q. Zeng, H. Zhang, X. Liu, Z. Wang, Y. Wu, Recent developments in research of double glow plasma surface alloying technology: a brief review, *J. Mater. Res. Technol.* 9 (2020) 6859–6882, <https://doi.org/10.1016/j.jmrt.2020.03.123>.
- [24] A. Munitz, S. Salhov, S. Hayun, N. Frage, Heat treatment impacts the microstructure and mechanical properties of AlCoCrFeNi high entropy alloy, *J. Alloys Compd.* 683 (2016) 221–230, <https://doi.org/10.1016/j.jallcom.2016.05.034>.
- [25] K.R. Lim, K.S. Lee, J.S. Lee, J.Y. Kim, H.J. Chang, Y.S. Na, Dual-phase high-entropy alloys for high-temperature structural applications, *J. Alloys Compd.* 728 (2017) 1235–1238, <https://doi.org/10.1016/j.jallcom.2017.09.089>.
- [26] P. Shi, Y. Yu, N. Xiong, M. Liu, Z. Qiao, G. Yi, Q. Yao, G. Zhao, E. Xie, Q. Wang, Microstructure and tribological behavior of a novel atmospheric plasma sprayed AlCoCrFeNi high entropy alloy substrate self-lubricating composite coatings, *Tribology International* 151 (2020) 106470, <https://doi.org/10.1016/j.triboint.2020.106470>.
- [27] D.-Q. Doan, V.-H. Nguyen, T.-V. Tran, M.-T. Hoang, Atomic-scale analysis of mechanical and wear characteristics of AlCoCrFeNi high entropy alloy coating on Ni substrate, *J. Mat. Process. Technol.* 85 (2023) 1010–1023, <https://doi.org/10.1016/j.jmapro.2022.12.009>.
- [28] Q. Fan, C. Chen, C. Fan, Z. Liu, X. Cai, S. Lin, C. Yang, Ultrasonic induces grain refinement in gas tungsten arc cladding AlCoCrFeNi high-entropy alloy coatings, *Mater. Sci. Eng. A* 821 (2021) 141607, <https://doi.org/10.1016/j.msea.2021.141607>.
- [29] A. Meghwal, A. Anupam, V. Luzin, C. Schulz, C. Hall, B.S. Murty, R.S. Kottada, C. Berndt, A.S.M. Ang, Multiscale mechanical performance and corrosion behaviour of plasma sprayed AlCoCrFeNi high-entropy alloy coatings, *J. Alloys Compd.* 854 (2021) 157140, <https://doi.org/10.1016/j.jallcom.2020.157140>.
- [30] D.M. Kemény, N. Miskolcziné Pálfi, É. Fazakas, Examination of microstructure and corrosion properties of novel AlCoCrFeNi multicomponent alloy, *Materials Today: Proceedings* 45 (2021) 4250–4253, <https://doi.org/10.1016/j.matpr.2020.12.285>.
- [31] Z. Chong, Y. Sun, W. Cheng, C. Han, L. Huang, C. Su, L. Jiang, Enhanced wear and corrosion resistances of AlCoCrFeNi high-entropy alloy coatings via high-speed laser cladding, *Mater. Today Commun.* 33 (2022) 104417, <https://doi.org/10.1016/j.mtcomm.2022.104417>.
- [32] J. Zhang, S. Ma, Y. Xiong, B. Xu, S. Zhao, Elemental partitions and deformation mechanisms of L12-type multicomponent intermetallics, *Acta Mater.* 219 (2021) 117238, <https://doi.org/10.1016/j.actamat.2021.117238>.
- [33] L. Fan, T. Yang, Y. Zhao, J. Luan, G. Zhou, H. Wang, Z. Jiao, C.-T. Liu, Ultrahigh strength and ductility in newly developed materials with coherent nanolamellar architectures, *Nat. Commun.* 11 (2020) 6240, <https://doi.org/10.1038/s41467-020-20109-z>.
- [34] Y.Y. Zhao, H.W. Chen, Z.P. Lu, T.G. Nieh, Thermal stability and coarsening of coherent particles in a precipitation-hardened (NiCoFeCr)94Ti2Al4 high-entropy alloy, *Acta Mater.* 147 (2018) 184–194, <https://doi.org/10.1016/j.actamat.2018.01.049>.
- [35] Y. Ren, H. Wu, B. Liu, Q. Shan, S. Guo, Z. Jiao, I. Baker, A novel L12-strengthened AlCoCuFeNi high-entropy alloy with both high hardness and good corrosion resistance, *Mater. Lett.* 331 (2023) 133339, <https://doi.org/10.1016/j.matlet.2022.133339>.
- [36] Z. Lin, M. Li, J. Wang, Y. Zhou, Microstructure and high-temperature corrosion behavior of a Cr-Al-C composite, *J. Am. Ceram. Soc.* 90 (2007) 3930–3937, <https://doi.org/10.1111/j.1551-2916.2007.02059.x>.
- [37] X. Zou, M. Rachakonda, S. Chu, X. Zhao, J. Joardar, K.M. Reddy, Structure and mechanical properties of nanostructured rhombohedral Cr5Al8, *Mater Charact* 172 (2021) 110862, <https://doi.org/10.1016/j.matchar.2020.110862>.
- [38] Y. Shi, B. Yang, X. Xie, J. Brechtl, K.A. Dahmen, P.K. Liaw, Corrosion of Al_xCoCrFeNi high-entropy alloys: Al-content and potential scan-rate dependent pitting behavior, *Corros. Sci.* 119 (2017) 33–45, <https://doi.org/10.1016/j.corsci.2017.02.019>.
- [39] A. Erdogan, K.M. Döleker, S. Zeytin, Effect of laser re-melting on electric current assistive sintered CoCrFeNiAlxTiy high entropy alloys: formation, micro-hardness and wear behaviors, *Surf. Coat. Technol.* 399 (2020) 126179, <https://doi.org/10.1016/j.surfcoat.2020.126179>.

- [40] X. Chen, P. Zhang, D. Wei, H. Zhao, X. Wei, F. Ding, Tribological behavior of aluminum slurry coating on 300M steel, *J. Mater. Eng. Perform.* 26 (2017) 3719–3727, <https://doi.org/10.1007/s11665-017-2820-6>.
- [41] C.B. Nascimento, U. Donatus, C.T. Ríos, R.A. Antunes, Passive film composition and stability of CoCrFeNi and CoCrFeNiAl high entropy alloys in chloride solution, *Mater. Chem. Phys.* 267 (2021) 124582, <https://doi.org/10.1016/j.matchemphys.2021.124582>.
- [42] F. Abdi, H. Aghajani, S.K. Asl, Evaluation of the corrosion resistance of AlCoCrFeMnNi high entropy alloy hard coating applied by electro spark deposition, *Surf. Coat. Technol.* 454 (2023) 129156, <https://doi.org/10.1016/j.surfcoat.2022.129156>.
- [43] F. Abdi, H. Aghajani, A. Taghizadeh Tabrizi, L. Nasimi, F. Fazli Shokouhi, Study on the effect of the crack closing of AlCoCrFeMnNi high entropy alloy electro-spark deposited coating by plasma nitriding on the corrosion resistance, *J. Alloys Compd.* 966 (2023) 171629, <https://doi.org/10.1016/j.jallcom.2023.171629>.
- [44] W. Chai, T. Lu, Y. Pan, Corrosion behaviors of FeCoNiCr_x ($x = 0, 0.5, 1.0$) multi-principal element alloys: role of Cr-induced segregation, *Intermetallics* 116 (2020) 106654, <https://doi.org/10.1016/j.intermet.2019.106654>.
- [45] Y. Garip, N. Ergin, O. Ozdemir, Resistance sintering of CoCrFeNiAl_x ($x = 0.7, 0.85, 1$) high entropy alloys: microstructural characterization, oxidation and corrosion properties, *J. Alloys Compd.* 877 (2021) 160180, <https://doi.org/10.1016/j.jallcom.2021.160180>.
- [46] M.L. Zheludkevich, K.A. Yasakau, A.C. Bastos, O.V. Karavai, M.G.S. Ferreira, On the application of electrochemical impedance spectroscopy to study the self-healing properties of protective coatings, *Electrochim. Commun.* 9 (2007) 2622–2628, <https://doi.org/10.1016/j.elecom.2007.08.012>.
- [47] M.L. Zheludkevich, R. Serra, M.F. Montemor, I.M.M. Salvado, M.G.S. Ferreira, Corrosion protective properties of nanostructured sol-gel hybrid coatings to AA2024-T3, *Surf. Coat. Technol.* 200 (2006) 3084–3094, <https://doi.org/10.1016/j.surfcoat.2004.09.007>.
- [48] Y. Lou, W. Chang, T. Cui, J. Wang, H. Qian, L. Ma, X. Hao, D. Zhang, Microbiologically influenced corrosion inhibition mechanisms in corrosion protection: a review, *Bioelectrochemistry* 141 (2021) 107883, <https://doi.org/10.1016/j.bioelechem.2021.107883>.